*Int. J. Appl. Math. Comput. Sci.*, , Vol. , No. , –
DOI:

amcs

# A DYNAMICALLY ADAPTIVE LATTICE BOLTZMANN METHOD FOR THERMAL CONVECTION PROBLEMS

KAI FELDHUSEN [a,b], RALF DEITERDING [c,*], CLAUS WAGNER [a,b]

[a]Institute of Aerodynamics and Flow Technology
German Aerospace Center (DLR), 37073 Göttingen, Germany

[b]Institute of Thermo- and Fluiddynamics
Technische Universität Ilmenau, 98693 Ilmenau, Germany

[c]Aerodynamics and Flight Mechanics Research Group
University of Southampton, Highfield Campus, Southampton SO17 1BJ, United Kingdom
email: r.deiterding@soton.ac.uk

Utilizing the Boussinesq approximation, a double-population incompressible thermal lattice Boltzmann method (LBM) for forced and natural convection in two and three space dimensions is developed and validated. A block-structured dynamic adaptive mesh refinement (AMR) procedure tailored for LBM is applied to enable computationally efficient simulations of moderate to high Rayleigh number flows which are characterized by a large scale disparity in boundary layers and free stream flow. As test cases, the analytically accessible problem of a two-dimensional (2D) forced convection flow through two porous plates and the non-Cartesian configuration of a heated rotating cylinder are considered. The objective of the latter is to advance the boundary conditions for accurate treatment of curved boundaries and to demonstrate the effect on the solution. The effectiveness of the overall approach is demonstrated for the natural convection benchmark of a 2D cavity with differentially heated walls at Rayleigh numbers from $10^3$ up to $10^8$. To demonstrate the benefit of the used AMR procedure for three-dimensional (3D) problems, results from the natural convection in a cubic cavity at Rayleigh numbers from $10^3$ up to $10^5$ are compared with benchmark results.

**Keywords:** Lattice Boltzmann method, adaptive mesh refinement, thermal convection, incompressible

## 1. Introduction

In recent years, the lattice Boltzmann method (LBM) has emerged as a powerful alternative to traditional Navier-Stokes (NS) solvers (Chen and Doolen, 1998) to predict thermal fluid flow (Guo *et al.*, 2002; Kuznik *et al.*, 2007; Peng *et al.*, 2003), turbulent fluid flow (Jonas *et al.*, 2006), multiphase fluid flow (Lee and Lin, 2005; Yu and Fan, 2009) and magnetohydrodynamics (Deller, 2002). Instead of discretizing the NS equations directly, the LBM is based on solving a simplified version of the Boltzmann equation in a specifically chosen discrete phase space. Using a Chapman-Enskog expansion, it has been shown that the approach recovers the NS equations in the limit of a vanishing Knudsen number (Hähnel, 2004). Originally proposed for

*Corresponding author

the isothermal weakly compressible case, several method enhancements for incompressibility (He and Luo, 1997; Qian *et al*., 1992) as well as incorporation of a buoyancy-driven temperature field for thermal convection flows are available (He *et al*., 1998; Qian, 1993). In general, there are two different categories of thermal lattice Boltzmann models. For the multispeed approach, the number of discrete velocity directions will be increased and the equilibrium distribution function is supplemented by higher order velocity terms to solve the internal energy equation, cf. (McNamara and Alder, 1993; Alexander *et al*., 1993; Qian, 1993). However, this model is reported to exhibit numerical instabilities, cf. (Chen and Teixeira, 2000). Here, we have chosen to pursue the strictly incompressible double distribution function (DDF) approach proposed by Guo *et al*. (2002) for 2D and the straightforward expansion to 3D by He *et al*. (2004) and Azwadi Che Sidik and Syahrullail (2009).

While the original LBM is formulated on a uniform Cartesian grid, an increase of local resolution is particularly necessary in the thermal boundary layers close to heated objects and walls. Kuznik *et al*. (2007) and Peng *et al*. (2003) demonstrated the computational benefit of a non-uniform grid for a thermal DDF LBM method in two and three spatial dimensions for simulating thermal convection in Cartesian cavities. In both works, a static geometry transformation is applied to the discretization in order to stretch the Cartesian lattice in the cavity center and reduce the spacing continuously towards the walls. Solution adaptive meshing is not used and on-the-fly mesh adaptation seems to have been applied so far to DDF LBM methods only in the context of isothermal two-phase flows, cf. (Yu and Fan, 2009). Our objective in this paper is to close this gap. We supplement a thermal DDF LBM method with solution adaptive, dynamic mesh refinement. While adaptive lattice Boltzmann methods in the past have used primarily isotropic refinement of individual cells, cf. (Chen *et al*., 2006), we apply in here a block-based approach, which is more suitable for the regular transport step of the LBM and thereby computationally significantly more efficient. The underlying data structures including distributed memory parallelization are borrowed from the finite volume mesh refinement system AMROC (Deiterding, 2011). In order to fit smoothly into AMROC, the DDF LBM is formulated on cell-centered data structures and not node-based as it is mainly used for LBM in order to simplify the implementation of physical boundary conditions. In addition, complex geometry boundary condition treatment for possibly moving structures is incorporated. The update of the non-uniform lattice and the dynamic refinement procedure are orchestrated with the recursive Berger-Collela algorithm (Berger and Colella, 1988). While the efficiency of this algorithm is undisputed for time-explicit finite volume schemes, its application to LBM is a novelty. In summary, our adaptive method is uniquely designed for the efficient simulation of real-world thermal flow problems. In this paper, the underlying computational techniques are described and the required validation for well-understood thermal convection problems is provided.

In Section 2, we discuss the details of the numerical method, including the advanced thermal lattice Boltzmann approach, the block-based AMR method and the treatment of geometrically complex boundaries in the originally Cartesian scheme. Section 3 presents the computational results, where the analytic solution of the 2D flow between two moving porous plates, the 2D flow around a rotating heated cylinder and the well-known benchmark case of a two-dimensional cavity with differentially heated walls are considered. The result section is closed presenting the solution of the flow in a 3D cubic cavity with differentially heated walls. The conclusions including a short outlook are given in Section 4.

## 2. Numerical method

**2.1. Thermal lattice Boltzmann scheme.** The incompressible two-dimensional LBM constructed under Boussinesq approximation used in the present work has been proposed by Guo *et al*. (2002). For the three-dimensional case the incompressible LBM operator by

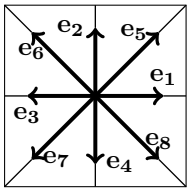


Fig. 1. Numerical stencil of D2Q9 - Discrete velocity directions in a computational cell.

He *et al*. (2004) is applied. By using the Bhatnagar-Gross-Krook (BGK) collision model (Bhatnagar *et al*., 1954), the lattice Boltzmann equation for the partial probability distribution function $f_i$ with force field term $F_i$ can be formulated as

$$f_i\left(\mathbf{x}+c\mathbf{e}_i\Delta t, t+\Delta t\right) = f_i\left(\mathbf{x},t\right) - \frac{1}{\tau_\nu}\left(f_i\left(\mathbf{x},t\right) - f_i^{(eq)}\left(\mathbf{x},t\right)\right) + \Delta t F_i. \quad (1)$$

In the DDF approach, a set of corresponding lattice Boltzmann equations

$$g_i\left(\mathbf{x}+c\mathbf{e}_i\Delta t, t+\Delta t\right) = g_i\left(\mathbf{x},t\right) - \frac{1}{\tau_\mathcal{D}}\left(g_i\left(\mathbf{x},t\right) - g_i^{(eq)}\left(\mathbf{x},t\right)\right) \quad (2)$$

is introduced based on distribution functions $g_i$ that are used to convect the macroscopic scalar quantity, here temperature, with the flow field. In the latter, $\mathbf{e}_i$ is the unit velocity vector in direction of the $i$th discrete velocity space direction, $t$ and $\Delta t$ denote the time and time step, $x$ the position, $\Delta x$ the spatial increment, and $c = \Delta x/\Delta t$ is the particle speed. The relaxations times are $\tau_\nu$ for the flow field and $\tau_\mathcal{D}$ for the temperature field. The respective equilibrium distribution functions are denoted by $f_i^{(eq)}$ and $g_i^{(eq)}$. In the two-dimensional case, a model with nine discrete unit velocities is used to compute the flow field (D2Q9) and an operator with four discrete velocities for the temperature field (D2Q4). The orientation of the discrete unit length velocities $\mathbf{e}_i$ used to compute the velocity fields are depicted in Fig. 1. In the three-dimensional case, an operator with nineteen unit velocities is used for the flow field (D3Q19) and a model with six discrete velocities for the temperature field (D3Q6). The extended version of the orientation of the discrete unit length velocities $\mathbf{e}_i$ are given in (3).

$$\mathbf{e}_i = \begin{cases} (0,0) & i=0, \\ (\pm1,0,0),(0,\pm1,0),(0,0,\pm1) & i=1,...,6, \\ (\pm1,\pm1,0),(\pm1,0,\pm1),(0,\pm1,\pm1) & i=7,...,18 \end{cases} \quad (3)$$

The basic LBM algorithm is divided into the steps of transport (or streaming) and collision, which are applied basically identically to (1) and (2). The following transport step represents the advection of fluid particles along the corresponding discrete velocities and is

$$\mathcal{T}: \quad \tilde{f}_i\left(\mathbf{x}+c\mathbf{e}_i\Delta t, t+\Delta t\right) = f_i\left(\mathbf{x},t\right). \quad (4)$$

Relaxation of the distribution functions towards the local equilibrium is performed on the transported distribution functions in the collision step

$$\mathcal{C}: \quad f_i\left(\cdot, t+\Delta t\right) = \tilde{f}_i\left(\cdot, t+\Delta t\right) - \frac{1}{\tau_\nu}\left(\tilde{f}_i\left(\cdot,t\right) - \tilde{f}_i^{(eq)}\left(\cdot,t\right)\right). \quad (5)$$

With the pressure $p$ and the velocity vector $\mathbf{u}$ as independent variables, the specific equilibrium distribution function $f_i^{(eq)}$ for the D2Q9 model is defined as (Guo *et al*., 2002)

$$f_i^{(eq)} = \begin{cases} -4\sigma\frac{p}{c^2} - s_i(\mathbf{u}), & \text{for } i=0, \\ \lambda\frac{p}{c^2} + s_i(\mathbf{u}), & \text{for } i=1,...,4, \\ \gamma\frac{p}{c^2} + s_i(\mathbf{u}), & \text{for } i=5,...,8, \end{cases} \quad (6)$$

where the parameters $\sigma$, $\lambda$, and $\gamma$ satisfy $\lambda+\gamma = \sigma$ and $\lambda + 2\gamma = 1/2$. The functions $s_i(\mathbf{u})$ depend on the macroscopic velocity vector $\mathbf{u}$ and the discrete velocity vector $\mathbf{e}_i$ and obey

$$s_i\left(\mathbf{u}\right) = \omega_i\left[3\frac{\mathbf{e}_i\cdot\mathbf{u}}{c} + 4.5\frac{\left(\mathbf{e}_i\cdot\mathbf{u}\right)^2}{c^2} - 1.5\frac{|\mathbf{u}|^2}{c^2}\right], \quad (7)$$

where the coefficients are given by $\omega_0 = 4/9, \omega_{1,...,4} = 1/9$, and $\omega_{5,...,8} = 1/36$. Using (6) and (7), the macroscopic values for velocity and dynamic pressure are given as

$$\mathbf{u} = \sum_{i>0} c\mathbf{e}_i f_i, \quad p = \frac{c^2}{4\sigma}\left[\sum_{i>0} f_i + s_0(\mathbf{u})\right]. \quad (8)$$

For the D3Q19 model the parameters change to $\sigma = 1/2$, $\lambda = 1/18$, and $\gamma = 1/36$. Furthermore the weight coefficients are given by $\omega_0 = 1/3, \omega_{1,\dots,6} = 1/18$, and $\omega_{7,\dots,18} = 1/36$. For the D2Q4 model used to compute the temperature field, the equilibrium function $g_i^{(eq)}$ is

$$g_i^{(eq)} = \frac{T}{4}\left[1 + 2\frac{\mathbf{e}_i \cdot \mathbf{u}}{c}\right], \quad \text{for } i = 1, \dots, 4 \quad (9)$$

and the macroscopic temperature is $T = \sum_{i=1}^{4} g_i$. Analogously, in the D3Q6 model of the temperature field, the equilibrium function reads

$$g_i^{(eq)} = \frac{T}{6}\left[1 + 3\frac{\mathbf{e}_i \cdot \mathbf{u}}{c}\right], \quad \text{for } i = 1, \dots, 6 \quad (10)$$

and the macroscopic temperature $T = \sum_{i=1}^{6} g_i$. Since the fluid is assumed to be incompressible, a linear dependency between temperature differences and gravitational forces is applied (Boussinesq approximation), cf. (Mohamad and Kuzmin, 2010), which leads to the force term $F_i$. The force in (11) acts only in the two direct vertical directions. For 2D, this can be expressed according to Fig. 1 (Guo *et al*., 2002) as

$$F_i = \frac{1}{2}\left(\delta_{i2} + \delta_{i4}\right)\mathbf{e}_i \cdot \mathbf{F} \quad (11)$$

with

$$\mathbf{F} = \mathbf{g}\beta\left(T - T_{ref}\right), \quad (12)$$

where $\mathbf{g}$ and $\beta$ are the acceleration vector of gravity and the coefficient of thermal expansion, respectively; $T_{ref}$ is the average temperature. The force term establishes the coupling between the lattice Boltzmann equations for the flow field (1) and the temperature field (2).

Note that through a multiscale Chapman-Enskoq expansion, the incompressible Navier-Stokes equations can be derived from the discussed incompressible LBGK model. After neglecting the viscous heat dissipation and compression work carried out by the pressure, the temperature field obeys a passive scalar equation. In sum, the approximated incompressible equations in this work are, cf. (Guo *et al*., 2002),

$$\nabla \cdot \mathbf{u} = 0, \quad (13)$$

$$\frac{\partial \mathbf{u}}{\partial t} + \nabla \cdot (\mathbf{u}\mathbf{u}) = -\nabla p + \nu \nabla^2 \mathbf{u} + \mathbf{F}, \quad (14)$$

$$\frac{\partial T}{\partial t} + \nabla \cdot (\mathbf{u}T) = \mathcal{D}\nabla^2 T. \quad (15)$$

The kinematic viscosity $\nu$ and the thermal diffusivity $\mathcal{D}$ are related to the dimensionless collision times by $\nu = \frac{1}{6}\left(2\tau_\nu - 1\right)c\Delta x$ and $\mathcal{D} = \frac{1}{4}\left(2\tau_\mathcal{D} - 1\right)c\Delta x$. Introducing the physical speed of sound as $c_s = c/\sqrt{3}$ these expressions yield the relations

$$\tau_\nu = \frac{\nu + c_s^2 \Delta t/2}{c_s^2 \Delta t}, \quad \tau_\mathcal{D} = \frac{\mathcal{D} + \frac{3}{2}c_s^2 \Delta t/2}{\frac{3}{2}c_s^2 \Delta t}, \quad (16)$$

which can be used to evaluate the dimensionless collision times in (1) and (2) for given macroscopic gas properties $\nu$, $\mathcal{D}$ and time step $\Delta t$.

**2.2. Adaptive mesh refinement.** For local dynamic mesh adaptation we have adopted the block-structured AMR method proposed by Berger and Colella (1988). This method was originally designed for time-explicit finite volume schemes for hyperbolic conservation laws, however, its recursive execution procedure and natural consideration of time step refinement make it equally applicable to lattice Boltzmann schemes, which is is not surprising as a hyperbolic constant velocity advection equation is the theoretical underpinning of the transport step (4). In order to fit smoothly into our existing, fully parallelized finite volume AMR software system AMROC (Deiterding, 2011), we have implemented the LBM cell-based. In the block-based AMR approach, finite volume cells are clustered with a special algorithm into non-overlapping rectangular grids. The grids have a suitable layer of halo cells for synchronization and applying inter-level and physical boundary conditions. Refinement levels are integrated recursively starting from the coarsest level. With index $l$ denoting the AMR level, the spatial mesh width $\Delta x_l$ and the time step $\Delta t_l$ are refined by the same factor $r_l$, where we assume $r_l \geq 2$ for $l > 0$ and

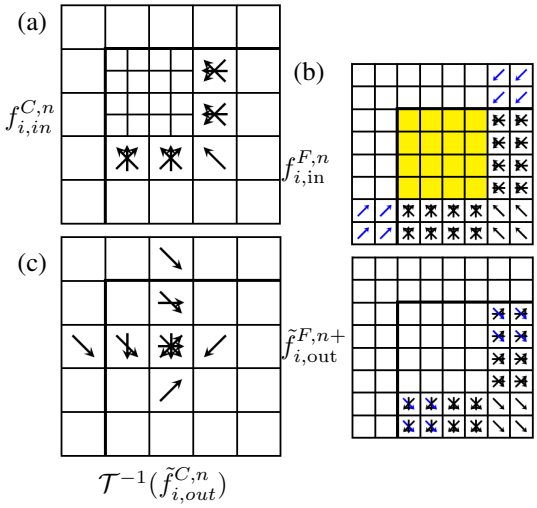


Fig. 2. Visualization of distributions involved in data exchange at a coarse ($C$) - fine ($F$) boundary. The thick black lines indicate a physical boundary. (a) Coarse distributions going into fine grid; (b) incoming interpolated fine distributions in halos (top), outgoing distributions in halos after two fine-level transport steps (bottom); (c) averaged distributions replacing coarse values before update is repeated in cells next to boundary.

$r_0 = 1$. In the adaptive thermal LBM, it is of foremost importance that the dimensionless collision times of the DDF LBM are adjusted on a level basis according to (16) as the time step is recursively refined. In addition, the interface region requires a specialized treatment to ensure consistent transport of coarse-grid distributions into refined cells and of fine-grid distributions into the coarse cells adjacent to the boundaries of refined regions. Since the D2Q4 stencil is just a simplified version of the D2Q9 method, we restrict our description of the interface algorithm to the latter. Distinguishing between the transport and collision operators, $\mathcal{T}$ and $\mathcal{C}$, respectively (cf. (4) and (5)), our method proceeds in the following steps if a refinement factor of 2 is considered:

1. Complete update on coarse grid: $f_i^{C,n+1} := \mathcal{C}\mathcal{T}(f_i^{C,n})$

2. Use coarse grid distributions $f_{i,\text{in}}^{C,n}$ that propagate into the fine grid, cf. Fig. 2(a), to construct initial fine grid halo values $f_{i,\text{in}}^{F,n}$, cf. Fig. 2(b).

3. Complete transport $\tilde{f}_i^{F,n} := \mathcal{T}(f_i^{F,n})$ on whole fine mesh. Collision $f_i^{F,n+1/2} := \mathcal{C}(\tilde{f}_i^{F,n})$ is applied only in the interior cells (yellow in Fig. 2(b)).

4. Repeat 3. to obtain $\tilde{f}_i^{F,n+1/2} := \mathcal{T}(f_i^{F,n+1/2})$ and $f_i^{F,n+1} := \mathcal{C}(\tilde{f}_i^{F,n+1/2})$.

5. Average outgoing distributions from fine grid halos (Fig. 2(c)), that is $\tilde{f}_{i,\text{out}}^{F,n+1/2}$ in the inner halo layer and $\tilde{f}_{i,\text{out}}^{F,n}$ (outer halo layer) to obtain $\tilde{f}_{i,\text{out}}^{C,n}$.

6. Revert transport for averaged outgoing distributions, $\bar{f}_{i,\text{out}}^{C,n} := \mathcal{T}^{-1}(\tilde{f}_{i,\text{out}}^{C,n})$, and overwrite those in the previous coarse grid time step.

7. Synchronization of $f_i^{C,n}, \bar{f}_{i,\text{out}}^{C,n}$ on entire level.

8. Repeat complete update on coarse grid cells next to coarse-fine boundary only: $f_i^{C,n+1} := \mathcal{C}\mathcal{T}(f_i^{C,n}, \bar{f}_{i,\text{out}}^{C,n})$

In this description and in Fig. 2, the time steps on the coarse level $C$ are indexed by the superscript $n$, index $F$ denotes the fine level and the subscripts $\text{in}$ and $\text{out}$ indicate distributions which are convected in- and outwards of the fine grid along the coarse-fine boundary. The overall algorithm is computationally equivalent to the method by Chen *et al.* (2006) but explicitly tailored to the Berger-Collela recursion that updates coarse grids in their entirety before fine grids are computed. The complete update of the entire respective coarse mesh and subsequent correction is the basis of the computational efficiency of the Berger-Collela method; however, this approach has so far hardly been applied to lattice Boltzmann methods. Previous adaptive LBM, cf. (Chen *et al.*, 2006), update the fine grid before the respective coarse level and provide no apparent avenue for implementing time-interpolated fine level interface conditions. While not being used above, the benefit of interpolating in time the non-equilibrium portion of coarse-grid distributions crossing

the coarse-fine interface in Step 4 has been demonstrated by Dupuis and Chopard (2003) and will be considered in our implementation in the future.

**2.3. Wall boundary treatment.** The correct implementation of boundary condition is very important for numerical stability. For the considered test cases we need different implementations of boundary conditions for the velocity and temperature partial distribution functions. No-slip or adiabatic boundary conditions are realized via a bounce-back approach for the unknown partial distribution functions as described in (Succi, 2001). To prescribe fixed macroscopic values on the wall in form of Dirichlet boundary conditions we use a second order extrapolation scheme from Guo *et al*. (2002). The outflow boundary conditions are implemented via a linear propagation as prescribed in (Mohamad, 2011). We use a set of halo cells around the computational domain to manipulate the unknown partial probability distribution functions in the transport step.

**2.4. Curved boundary treatment.** We represent non-Cartesian boundaries implicitly on the adaptive Cartesian grid by utilizing a scalar level set function $\varphi$ that stores the distance to the boundary surface. The boundary surface is located exactly at $\varphi = 0$ and the boundary outer normal in every mesh point can be evaluated as $\mathbf{n} = -\nabla\varphi/|\nabla\varphi|$, (Deiterding, 2011). We treat a fluid cell as an embedded ghost cell if its *midpoint* satisfies $\varphi < 0$. In order to implement non-Cartesian boundary conditions with the LBM, we have chosen to pursue for now a 1st order accurate ghost fluid approach. In our technique, the density distributions in embedded ghost cells are adjusted to model the boundary conditions of a non-Cartesian reflective wall moving with velocity vector $\mathbf{w}$ before applying the unaltered LBM. The last step involves interpolation and mirroring of $p$, $T$, $\mathbf{u}$, across the boundary to $p'$, $T'$ and $\bar{\mathbf{u}}$ and modification of the macroscopic velocity vector in the immersed boundary cells to $\mathbf{u}' = 2\mathbf{w} - \bar{\mathbf{u}}$, cf. (Deiterding, 2011). From the newly constructed macroscopic values the distributions in the embedded ghost cells are simply set to $f_i^{eq}(p', \mathbf{u}')$ and $g_i^{eq}(T')$.

## 3. Results

For the setup of physical configurations it is useful to recall the definitions of the dimensionless Rayleigh and Prandtl number which is

$$\mathrm{Ra} = \frac{g\beta\Delta T H^3}{\nu\mathcal{D}}, \quad \mathrm{Pr} = \frac{\nu}{\mathcal{D}}. \tag{17}$$

The characteristic velocity $U$ for thermal convection flows is generally set to the buoyancy velocity $U = \sqrt{g\beta\Delta T H}$, where $H$ denotes a problem-dependent geometric height. A cell $(j,k)$ is flagged for refinement if any of the scaled gradient relations

$$\begin{aligned} &|\phi_{j+1,k} - \phi_{j,k}| > \epsilon_\phi, \quad |\phi_{j,k+1} - \phi_{j,k}| > \epsilon_\phi, \\ &|\phi_{j+1,k+1} - \phi_{j,k}| > \epsilon_\phi \end{aligned} \tag{18}$$

is satisfied for a particular macroscopic component $\phi_{j,k}$ and a prescribed limit $\epsilon_\phi$. If not stated otherwise, $\epsilon_T$ is set to $1\%$ of maximum temperature and $\epsilon_u$, $\epsilon_v$, $\epsilon_w$ are set to $5\%$ of characteristic velocity.

**3.1. Porous Plate.** In order to validate the basic numerical method, we selected the problem of forced thermal convection between two porous plates also employed by Guo *et al*. (2002). This problem is set up as a Couette flow between two porous plates of which the upper is in motion. A constant flow is injected normal to the lower plate and leaves the domain through the top plate with the same rate. The bottom plate is cooled, while the upper plate is heated. The analytic solutions for the horizontal velocity and the temperature profile in steady state are

$$u^*(y) = U_0 \left( \frac{e^{\mathrm{Re}\cdot y/H} - 1}{e^{\mathrm{Re}} - 1} \right), \tag{19}$$

$$T^*(y) = T_C + \Delta T \left( \frac{e^{\mathrm{RePr}\cdot y/H} - 1}{e^{\mathrm{RePr}} - 1} \right), \tag{20}$$

where $U_0$ is the velocity of the upper plate. The Reynolds number $\mathrm{Re}$ is based on the injection

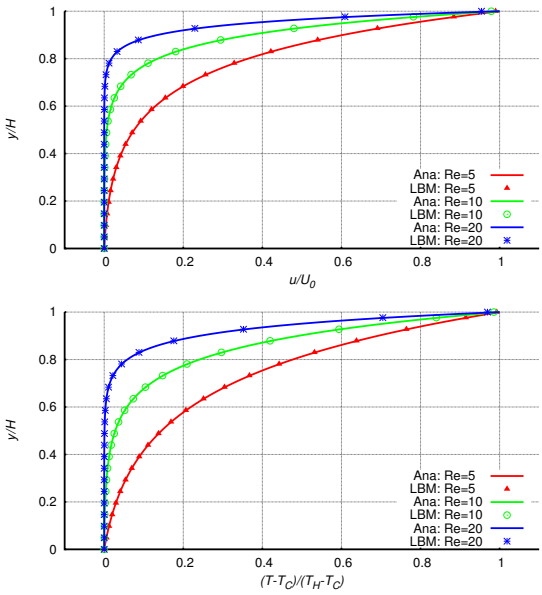


Fig. 3. Comparison of velocity and temperature distribution predicted for different Re in comparison with analytic solution.

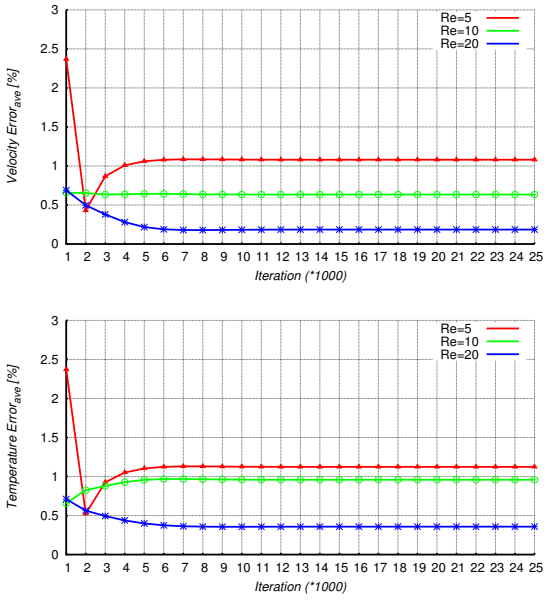


Fig. 4. Averaged L2-norm error for computed macroscopic velocity and temperature over iteration steps for different Re.

Table 1. Spatial averaged error: porous plate problem.

| Re | $E_{ave}(u)$ [%] | $E_{ave}(T)$ [%] |
|---|---|---|
| 5 | 1.08 | 1.14 |
| 10 | 0.64 | 0.98 |
| 20 | 0.19 | 0.38 |

velocity $V_0$ and is given by $\mathrm{Re} = \frac{V_0 \cdot H}{\nu}$. We study three different configurations with varying Reynolds number. The Prandtl number is fixed and set to $\mathrm{Pr} = 0.71$, which corresponds to air and the Rayleigh number is set to $\mathrm{Ra} = 100$. The velocity of the upper plate is also fixed and set to $U_0 = 0.1$. Finally, the dimensionless relaxation time $\tau_\nu$ on the coarsest level is prescribed as $\tau_\nu = 1/1.25$. The simulations are performed for the Reynolds numbers $\mathrm{Re} = 5, 10$ and $20$ using a base grid of $64 \times 32$ cells. Successive embedded static refinement with four additional levels with refinement factors $r_{1,\ldots,4} = 4$ is realized in the complete computational domain $[0, 64] \times [0, 32]$. In detail, we have the finest resolution $r_4$ near the top and bottom boundaries $[0, 64] \times ([0, 4] \,\&\, [28, 32])$, then $r_2$ in $[0, 64] \times ([4, 8] \,\&\, [24, 28])$ and $r_3$ in $[0, 64] \times ([8, 12] \,\&\, [20, 24])$. The coarsest refinement level $r_1$ is in the center region $[0, 64] \times [12, 20]$. The entire velocity field is initialized at rest as $(0, 0)^T$ and the temperature field to the constant value $T_C$. We compare the numerical predictions of the velocity and temperature distributions with the analytic solution. Figure 3 plots the normalized numerical results vs. the analytic solutions. From the point of validation, the macroscopic values for the horizontal velocity and scalar temperature are being calculated in each cell midpoint along each vertical line. The macroscopic values in the cells are averaged along the horizontal lines. The L2-norm error of the averaged macroscopic quantities $\Phi$ are calculated with (21) and displayed for the last iteration step in Table 1.

$$E_{ave}(\Phi) = \frac{\sqrt{\sum_i |\Phi_{ave}(\mathbf{x}_i) - \Phi^*(\mathbf{x}_i)|^2}}{\sqrt{\sum_i |\Phi^*(\mathbf{x}_i)|^2}} \qquad (21)$$

The agreement is obviously excellent and below 2% for all three cases. It is noteworthy that the error for the velocity is smaller than the one for the temperature. When increasing the

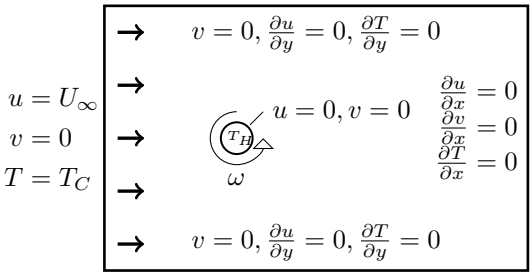


Fig. 5. Setup for the flow past the heated rotating cylinder.

discrete velocity directions for the temperature distribution functions from 6 to 9, this error should decrease. Figure 4 plots the averaged error for the computed macroscopic velocity and temperature over the computational iteration steps. The convergence to a fixed value is obvious.

**3.2. Fluid flow past a heated rotating cylinder.** In order to test the dynamic adaptation capabilities and boundary conditions for embedded complex geometries, we study the setup of a two-dimensional fluid flow past a heated isothermal rotating cylinder. The origin of the coordinate system is located in the center of the cylinder. As shown in Figure 5, the left boundary is an inlet with constant temperature $T_C$, zero vertical velocity and constant inflow velocity $U_\infty$. On the right hand side of the domain, an outlet is modeled by imposing zero horizontal gradient boundary conditions for velocity and temperature. Slip adiabatic wall boundary conditions are applied at the upper and lower boundary. The cylinder boundary is modeled as a no-slip wall, which is isothermally heated to the constant temperature $T_H$ and has the constant prescribed angular velocity $\Omega$. In terms of the cylinder radius $R = 15$, the computational domain has the extensions $[-6R, 16R] \times [-8R, 8R]$, which is sufficiently large to eliminate boundary influences on the solution (Yan and Zu, 2008). A base grid of $288 \times 240$ cells is used and three additional levels refined by the factors $r_1 = 2$ for level 1 and $r_{2,3} = 4$ for the other levels are applied. The dynamic refinement is based on scaled gradients of the velocity components as well as the temperature. The entire velocity field is initialized as $(U_\infty, 0)^T$ and the temperature field to the constant value $T_C$. The Reynolds number is given by $\mathrm{Re} = 2U_\infty R/\nu$ and is set to $\mathrm{Re} = 200$, where $U_\infty = 0.01$ is used. The peripheral velocity $V$ of the rotating cylinder is given by $V = \Omega R$. With the parameter $k = V/U_\infty = 0.5$ prescribed, we can determine $V$ and the angular velocity $\Omega$. To allow the direct comparison to the experimental results by Coutanceau and Menard (1985) the Prandtl number is set to $\mathrm{Pr} = 0.5$ and all variables are normalized with the reference length $R$ and $U_\infty$ as velocity. Further, $\frac{T-T_C}{T_H-T_C}$ defines the reference temperature and the time normalization factor follows as $R/U_\infty$. Figure 6 shows the dynamic adaption during the computation at four different time points by displaying streamlines and the domains of different mesh refinement levels. The onset of vortex shedding can be inferred. The finest refinement level (red) is located directly around the cylinder. Namely, where the boundary layers are located and detach from the cylinders surface. The unrefined regions, colored in blue, are in the outer regions of the domain. The refined levels move downstream with the shedding vortices and the cylinder wake increases over time.

Figure 7 compares the temporal evolution of the velocity components along representative points on the $x$-axis obtained in the simulation and with data from the experiment, while Fig. 8 displays the time evolution of the scalar temperature versus numerical results reported by Lai and Yan (2001). The latter adopted a finite volume method with non-orthogonal grids. Again, our simulation results are in good agreement with some differences in the $u$-velocity component at $t^* = 8$ when the vortex is shed (see Fig. 6). A possible explanation is our rather simple temperature operator with only four discrete unity directions and with the used boundary conditions for the curved boundary explained in Section 2.4. However, by using the bounce back scheme for curved moving boundaries from Bouzidi *et al.* (2001) and Li *et al.* (2013) with a global uniform mesh the differences are considerably reduced, cf. Fig. 9. Therefore, the next step is to implement the curved boundary treatment in the

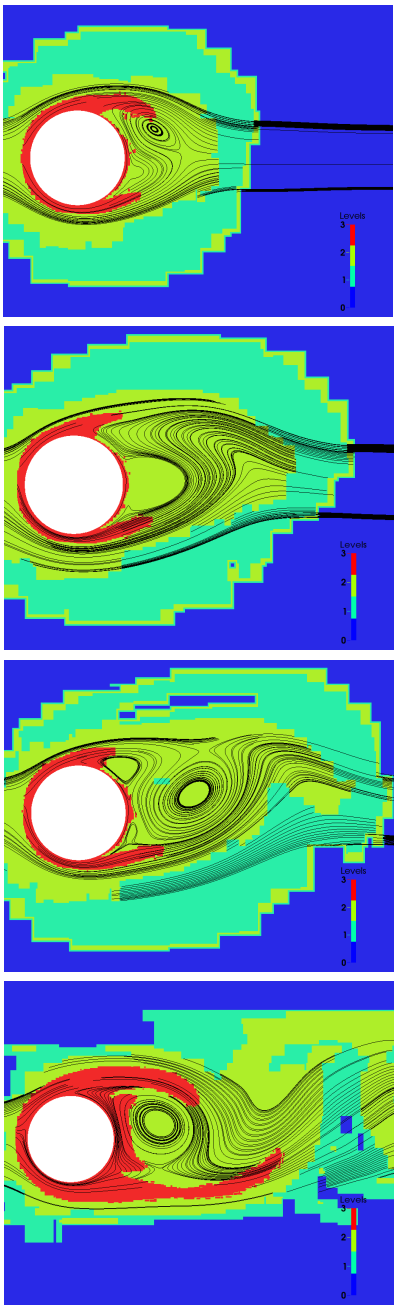


Fig. 6. Evolution of the velocity field and the adaptive mesh refinement regions for $\mathrm{Re} = 200$ and $k = 0.5$.

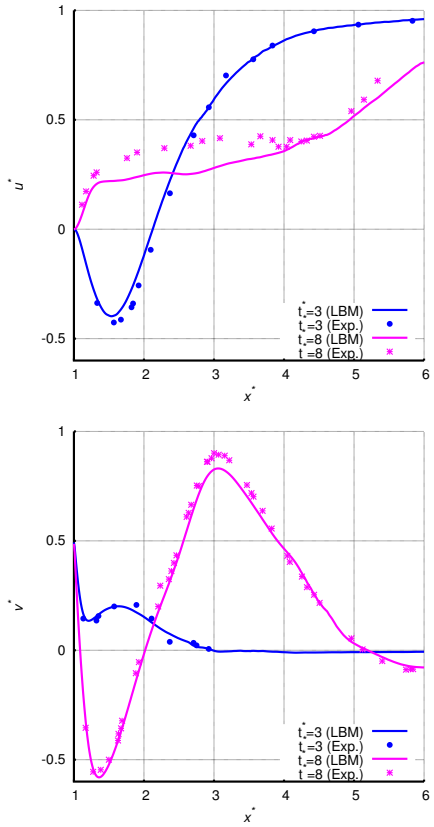


Fig. 7. Time evolution of the velocity components along the x-axis for $\mathrm{Re} = 200$ and $k = 0.5$.

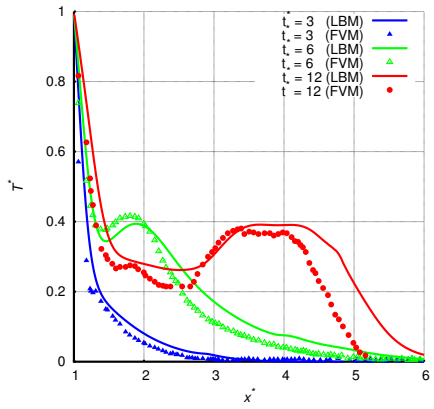


Fig. 8. Time evolution of the temperature along the x-axis for $\mathrm{Re} = 200$, $\mathrm{Pr} = 0.5$ and $k = 0.5$.

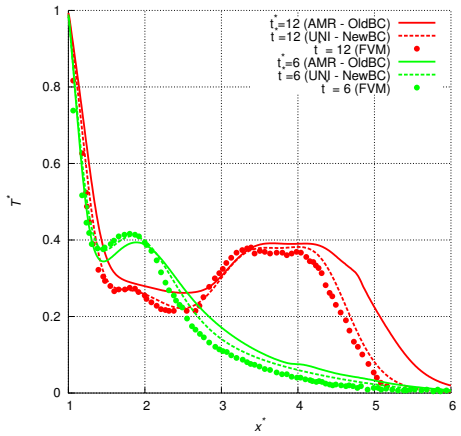


Fig. 9. Comparison of simulation results with different used curved boundary conditions: Time evolution of the Temperature along the x-axis for $\mathrm{Re} = 200$, $\mathrm{Pr} = 0.5$ and $k = 0.5$.

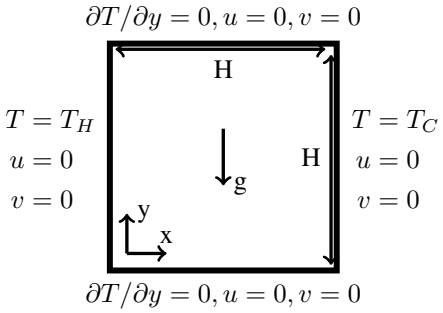


Fig. 10. Configuration of the two dimensional cavity.

AMR method.

### 3.3. Natural convection in a square 2D-cavity.

In order to benchmark the overall method we employ a two-dimensional square cavity with differentially heated walls. At the vertical walls isothermal temperatures $T_H$ and $T_C$ are prescribed and adiabatic boundary conditions are applied at top and bottom. Further, at all four walls we prescribe no-slip boundary conditions for the velocity field. Figure 10 depicts this setup. The flow is characterized by the Prandtl number $\mathrm{Pr} = 0.71$ (air) and the Rayleigh numbers $\mathrm{Ra} = 10^j$ with $j = 3, \ldots, 8$ with accordingly increasing velocities $U$. The reference temperature is given by $T_{ref} = (T_H + T_C)/2$. The simulations were terminated after reaching steady state. Two additional levels of refinement with $r_{1,2} = 2$ are used and the base mesh has $(H\Delta x_0)^2$ cells, whereby $\Delta x_0 = 1$ and $H$ is given in the left column of Table 2. For simulations with $\mathrm{Ra} = 10^3, \cdots, 10^6$ we use the defined refinement thresholds for horizontal and vertical velocity $\epsilon_u$, $\epsilon_v$ with $2.5\%$ of the characteristic velocity and $1\%$ of the maximum temperature. The thresholds for $\mathrm{Ra} = 10^7$ and $10^8$ remain as previously stated. We compare our adaptive simulation results to published reference data by De Vahl Davis (1983), who solved the NS equations on a uniform square mesh with a second order finite difference method, and by Guo *et al.* (2002), who used the incompressible thermal LBGK approach presented above with a uniform mesh. Further results by Kuznik *et al.* (2007), who used a D2Q9 DDF LBM approach with non-uniform mesh resolution, are listed in Table 2. Table 2 contains the obtained maximal horizontal velocity $u_{\max}$ along the vertical center line at $x = H/2$ and the location $y_{\max}$ of its occurrence and similarly for the horizontal center line at $y = H/2$, the maximal vertical velocity $v_{\max}$ and its location $x_{\max}$. Furthermore, the average Nusselt number

$$\mathrm{Nu}_{\mathrm{ave}} = -\int_0^H \frac{1}{\Delta T}\frac{\partial T}{\partial x}\bigg|_{x=0} dy \qquad (22)$$

is compared. Velocity values in Table 2 are normalized by the reference diffusion velocity $\mathcal{D}/H$. As expected, $u_{\max}$, $v_{\max}$ and $\mathrm{Nu}_{\mathrm{ave}}$ increase with increasing Rayleigh number $\mathrm{Ra}$. Comparing the $\mathrm{Nu}$ numbers predicted by our adaptive method to the literature data, an agreement within $2\,\%$ is found for all $\mathrm{Ra}$ numbers. Figure 11 shows the vertical velocity component in the horizontal mid-plane for all discussed Rayleigh numbers. The velocity profiles plotted in Fig. 11 reveal the development of a boundary layer close to the heated/cooled walls with velocity maxima/minima whose values increase/decrease with increasing/decreasing $\mathrm{Ra}$. This increase of the magnitude of the vertical velocity with increasing $\mathrm{Ra}$ is also reflected in Table 2. To give an impression of the flow solution, contours of the temperature fields and

Table 2. Comparison of the simulation results: natural convection in the square cavity.

| | Ref. | $u_{\max}$ | $y_{\max}$ | $v_{\max}$ | $x_{\max}$ | $\mathrm{Nu}_{\mathrm{ave}}$ |
|---|---|---|---|---|---|---|
| $\mathrm{Ra}=10^3$ | a | 3.640 | 0.810 | 3.688 | 0.180 | 1.115 |
| $U=0.01$ | b | 3.649 | 0.813 | 3.697 | 0.178 | 1.114 |
| $H=100$ | c | 3.655 | 0.813 | 3.699 | 0.180 | 1.115 |
| | d | 3.636 | 0.809 | 3.686 | 0.174 | 1.117 |
| $\mathrm{Ra}=10^4$ | a | 16.161 | 0.823 | 19.595 | 0.118 | 2.239 |
| $U=0.02$ | b | 16.178 | 0.823 | 19.617 | 0.119 | 2.245 |
| $H=150$ | c | 16.076 | 0.820 | 19.637 | 0.117 | 2.248 |
| | d | 16.167 | 0.821 | 19.597 | 0.120 | 2.246 |
| $\mathrm{Ra}=10^5$ | a | 34.666 | 0.855 | 68.457 | 0.066 | 4.504 |
| $U=0.05$ | b | 34.730 | 0.855 | 68.590 | 0.066 | 4.510 |
| $H=200$ | c | 34.834 | 0.859 | 68.267 | 0.062 | 4.535 |
| | d | 34.962 | 0.854 | 68.578 | 0.067 | 4.518 |
| $\mathrm{Ra}=10^6$ | a | 64.756 | 0.850 | 220.12 | 0.038 | 8.804 |
| $U=0.05$ | b | 64.630 | 0.850 | 219.360 | 0.038 | 8.806 |
| $H=200$ | c | 65.361 | 0.852 | 216.415 | 0.039 | 8.778 |
| | d | 64.133 | 0.860 | 220.537 | 0.038 | 8.792 |
| $\mathrm{Ra}=10^7$ | a | 140.255 | 0.887 | 702.45 | 0.021 | 16.429 |
| $U=0.05$ | d | 148.768 | 0.881 | 702.029 | 0.020 | 16.408 |
| $H=256$ | | | | | | |
| $\mathrm{Ra}=10^8$ | a | 297.145 | 0.945 | 2228.4 | 0.012 | 29.954 |
| $U=0.05$ | d | 321.457 | 0.940 | 2243.36 | 0.012 | 29.819 |
| $H=256$ | | | | | | |

a = Present (LBM-AMROC), b = (De Vahl Davis, 1983) (FDM - uniform), c = (Guo *et al.*, 2002) (LBM - uniform), d = (Kuznik *et al.*, 2007) (LBM - nonuniform).

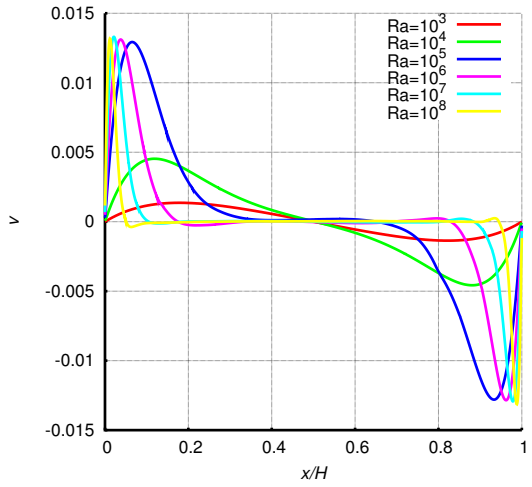


Fig. 11. Vertical velocity in the horizontal mid-plane of the 2D cavity for different Rayleigh numbers.

streamlines are presented in Fig. 12 for three considered $\mathrm{Ra}$ numbers. For all three $\mathrm{Ra}$ numbers the streamlines reflect that fluid rises at the heated wall and descends at the cooled wall. This generates a circulation around the center where the velocity is zero. For the lower $\mathrm{Ra}$ numbers the computed flow field are in good agreement with results reported in previous studies (De Vahl Davis, 1983; Guo *et al.*, 2002; Azwadi Che Sidik and Irwan, 2010; Kuznik *et al.*, 2007; Abdelhadi *et al.*, 2006). In the graph with the contours predicted for $\mathrm{Ra}=10^7$ the mesh refinement levels realized in the domain are additionally highlighted by colors. From the predominantly vertical isotherms obtained for the low $\mathrm{Ra}$ number case it can be concluded that the heat conduction dominates the heat transport between the heated walls. For larger $\mathrm{Ra}$ the isotherms are aligned more horizontally in the cavity's center due to the thinner boundary layers. The denser isotherms near the hot and cold wall further reflect the lower thermal boundary layer thickness for higher Rayleigh number. It is in this region where on-the-fly mesh resolution is particularly beneficial.

**3.4. Natural convection in a cubic cavity.** To benchmark the three-dimensional implementation of the method, we employ a 3D cubic cavity with differentially heated walls. As before, at the vertical walls the constant temperatures $T_H$ and $T_C$ are prescribed. At the bottom, top and front, back walls adiabatic boundary conditions are used for the temperature, while no-slip boundary conditions at all six walls are realized for the velocity fields. In summary, Fig. 13 represents this numerical setup. Again, the Prandtl number is $\mathrm{Pr}=0.71$ (air) and in the 3D simulations the Rayleigh numbers $\mathrm{Ra}=10^j$ is varied from $j=3,\ldots,5$. Here, we focus on the flow for $\mathrm{Ra}\leq 10^5$, since for higher $\mathrm{Ra}$ the flow is expected to become unsteady and eventually turbulent. To benchmark our method for a turbulent flow is however beyond the scope of this paper. As discussed above, the buoyancy (reference) velocity $U$ rises with increasing $\mathrm{Ra}$ and the reference temperature is given by $T_{ref}=(T_H+T_C)/2$. Two additional levels of refinement with $r_1=2$, $r_2=4$ are used and the base

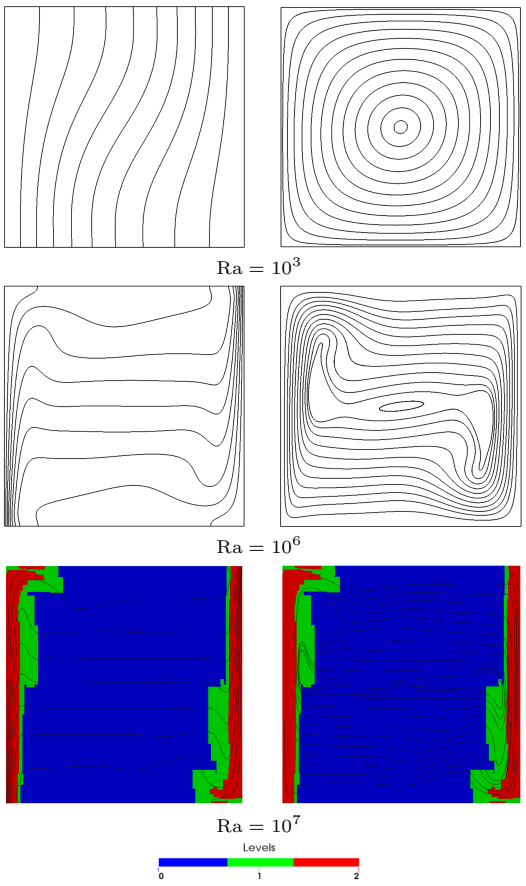


Fig. 12. LBM results of natural convective flow in the square cavity for three Ra numbers. Left: contours of isotherms. Right: streamlines.

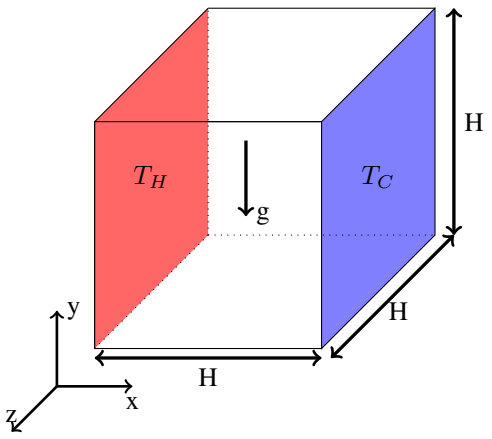


Fig. 13. Configuration of the three dimensional cavity.

mesh has $(H\Delta x_0)^3$ cells, whereby $\Delta x_0 = 1$ and $H$ is given in the left column of Table 3. The adaptive mesh refinement obeys the scaled gradient criteria given above in (18). The used thresholds for all three velocity components are 1%, 2% and 5% of the reference velocity $U$ for $\mathrm{Ra} = 10^3, 10^4$ and $10^5$, respectively. As before, 1% of $T_H$ is used as the temperature refinement threshold. The computed results are compared to published literature results after reaching steady state. Azwadi Che Sidik and Syahrullail (2009) use a D3Q19 DDF LBM approach with D3Q6 operator for the temperature field and a uniform cubic mesh to get excellent numerical stability and accuracy. Peng *et al.* (2003) use a three-dimensional incompressible LBM with DDF approach and two D3Q19 operators for the two fields and a non-uniform mesh resolution. Finally, Fusegi *et al.* (1991) use a high-resolution, finite difference NS solver with a uniform mesh resolution result and obtain results which agree reasonably well with experimental measurements. Figure 14 visualizes the temperature isosurfaces in the cubic enclosure and the different mesh refinement levels in the symmetry plane for $\mathrm{Ra} = 10^4, 10^5$. Near the heated walls, the isosurfaces are predominantly vertical. Notice, that the isosurfaces in the center of the cavity become more horizontally with increasing Ra. The reason is that the thermal boundary layer is becoming thinner. This observation is similar to that in the previous chapter. Note that the shaping of the mesh refinement levels for $\mathrm{Ra} = 10^4$ is much more pronounced than for $\mathrm{Ra} = 10^5$. As in the previous chapter, we compare the results in the symmetry plane $z = H/2$ in terms of maximal horizontal velocity $u_{\max}$ along the vertical center line at $x = H/2$ and at the corresponding location $y_{\max}$ of its occurrence and similarly for the horizontal center line at $y = H/2$, the maximal vertical velocity $v_{\max}$ and its location $x_{\max}$. Furthermore, we use the average Nusselt number (22) for comparison. Our results are listed in Table 3. The velocity values in Table 3 are normalized with the reference velocity $U$. The Nusselt number increases with increasing Ra number, which means that the convective part of the heat transfer predominates the conduction. Comparing the Nu numbers predicted with our

Table 3. Comparison of the simulation results: natural convection in the cubic cavity.

| | Ref. | $u_{\max}$ | $y_{\max}$ | $v_{\max}$ | $x_{\max}$ | $\mathrm{Nu}_{\mathrm{ave}}$ |
|---|---|---|---|---|---|---|
| $\mathrm{Ra} = 10^3$ | a | 0.132 | 0.195 | 0.132 | 0.829 | 1.099 |
| $U = 0.01$ | e | 0.132 | 0.186 | 0.132 | 0.841 | 1.096 |
| $H = 81$ | f | 0.132 | 0.188 | 0.133 | 0.826 | 1.097 |
| | g | 0.131 | 0.200 | 0.132 | 0.833 | 1.105 |
| $\mathrm{Ra} = 10^4$ | a | 0.197 | 0.194 | 0.220 | 0.887 | 2.270 |
| $U = 0.02$ | e | 0.200 | 0.182 | 0.224 | 0.883 | 2.301 |
| $H = 81$ | f | 0.206 | 0.163 | 0.221 | 0.887 | 2.304 |
| | g | 0.201 | 0.183 | 0.225 | 0.883 | 2.302 |
| $\mathrm{Ra} = 10^5$ | a | 0.141 | 0.152 | 0.242 | 0.935 | 4.583 |
| $U = 0.1$ | e | 0.151 | 0.142 | 0.248 | 0.930 | 4.670 |
| $H = 91$ | f | 0.149 | 0.136 | 0.240 | 0.935 | 4.658 |
| | g | 0.147 | 0.145 | 0.247 | 0.935 | 4.646 |

a = Present (LBM-AMROC), e = Azwadi *et al.* (Azwadi Che Sidik and Syahrullail, 2009) (LBM - uniform), f = Peng *et al.* (Peng *et al.*, 2003) (LBM - nonuniform), g = Fusegi *et al.* (Fusegi *et al.*, 1991) (NS - uniform)

method to the literature, an agreement within $2\%$ is found for all three $\mathrm{Ra}$ numbers, although the comparison of the horizontal velocity component shows larger differences. The reason for this might be a lack of dynamic mesh refinement near the upper and bottom walls. The mesh refinement is more pronounced near the heated and cooled walls, where the thinner thermal boundary layers are located.

## 4. Conclusions

A novel two and three dimensional incompressible dynamically adaptive thermal lattice Boltzmann method on block-based hierarchical finite volume meshes with embedded complex geometric structures has been developed and validated. The agreement for a two-dimensional porous plate problem on a Cartesian grid is nearly perfect. Successful validation against analytic solutions of the Navier-Stokes equations, e.g., for a heated rotating cylinder for $\mathrm{Pr} = 0.5$ has been achieved. While for this particular example the deviations in velocity and temperature were found to increase over time, a possible improvement could be the implementation of a bounce-back boundary condition for curved boundaries. For the benchmark of a two-dimensional heated cavity with Rayleigh numbers from $\mathrm{Ra} = 10^3$ to $10^8$, the predictions are in good agreement

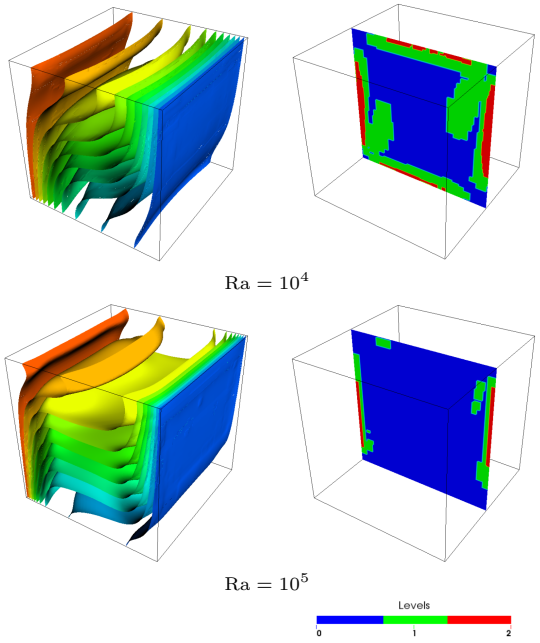


Fig. 14. Simulation results of natural convective flow in the cubic cavity. Left: isosurfaces of temperature. Color indicates temperature from hot (red) to cold (blue). Right: mesh refinement levels.

with published results. Our results in form of the computed Nusselt number reach an agreement within $2\%$. For higher Rayleigh numbers, the deviations in the considered quantities are greater in regions without refinement. The comparison for a three-dimensional heated cubic cavity with Rayleigh numbers from $\mathrm{Ra} = 10^3$ to $10^5$ against literature results delivers a good agreement as well. In terms of the Nusselt number, the agreement with literature results is again under $2\%$. A comprehensive analysis of CPU-time and memory savings by employing our unique block-based adaptive LBM will be conducted in the future. We will also take a closer look at how the results are influenced by the refinement criteria. Finally, extension and validation of the 3D approach to turbulent flows at higher $\mathrm{Ra}$ or $\mathrm{Re}$ numbers is planned.

## 5. Biographies

The author biographies will be provided upon acceptance.

## References


Abdelhadi, B., Hamza, G., Razik, B. and Raouache, E. (2006). Natural convection and turbulent instability in cavity, *WSEAS Transactions on Heat and Mass Transfer* **1(2)**: 179–184.

Alexander, F. J., Chen, S. and Sterling, J. D. (1993). Lattice boltzmann thermohydrodynamics, *Physical Review E* **47**: 2249–2252.

Azwadi Che Sidik, N. and Irwan, M. (2010). Simplified mesoscale lattice boltzmann numerical model for prediction of natural convection in a square enclosure filled with homogeneous porous media, *WSEAS Transactions on Fluid Mechanics* **3(5)**: 186–195.

Azwadi Che Sidik, N. and Syahrullail, S. (2009). A three-dimension double-population thermal lattice bgk model for simulation of natural convection heat transfer in a cubic cavity, *WSEAS Transactions on Mathematics* **8(9)**: 561–571.

Berger, M. and Colella, P. (1988). Local adaptive mesh refinement for shock hydrodynamics, *Journal of Computational Physics* **82**: 64–84.

Bhatnagar, P., Gross, E. and Krook, M. (1954). A model for collisional processes in gases I: small amplitude processes in charged and in neutral one-component systems, *Physical Review.* **94**: 511–525.

Bouzidi, M., Firdaouss, M. and Lallemand, P. (2001). Momentum transfer of a boltzmann-lattice fluid with boundaries, *Physics of Fluids* **13**: 3452.

Chen, H., Filippova, O., Hoch, J., Molvig, K., Shock, R., Teixeira, C. and Zhang, R. (2006). Grid refinement in lattice Boltzmann methods based on volumetric formulation, *Physica A* **362**: 158–167.

Chen, H. and Teixeira, C. (2000). H-theorem and origins of instability in thermal lattice boltzmann models, *Computer Physics Communications* **129(1)**: 21–31.

Chen, S. and Doolen, G. (1998). Lattice Boltzmann method for fluid flows, *Annual Review of Fluid Mechanics* **30**: 329–364.

Coutanceau, M. and Menard, C. (1985). Influence of rotation on the near-wake development behind an impulsively started circular cylinder, *Journal of Fluid Mechanics* **158**: 399–446.

De Vahl Davis, G. (1983). Natural convection of air in a square cavity a benchmark numerical solution, *International Journal for Numerical Methods in Fluids* **3**: 249–264.

Deiterding, R. (2011). Block-structured adaptive mesh refinement - theory, implementation and application, *ESAIM Proceedings* **34**: 97–150.

Deller, P. (2002). Lattice kinetic schemes for magnetohydrodynamics, *Journal of Computational Physics* **179(1)**: 95–126.

Dupuis, A. and Chopard, B. (2003). Theory and applications of an alternative lattice Boltzmann grid refinement algorithm, *Physica E* **67**: 066707.

Fusegi, T., Hyun, J., Kuwahara, K. and Farouk, B. (1991). A numerical study of three-dimensional natural convection in a differentially heated cubical enclosure, *International Journal of Heat and Mass Transfer* **34(6)**: 1543–1557.

Guo, Z., Shi, B. and Zheng, C. (2002). A coupled lattice BGK model for the Boussinesq equations, *International Journal for Numerical Methods in Fluids* **39**: 325–342.

Hähnel, D. (2004). *Molekulare Gasdynamik*, Springer.

He, N.-Z., Wang, N.-C., Shi, B.-C. and Guo, Z.-L. (2004). A unified incompressible lattice BGK model and its application to three-dimensional lid-driven cavity flow, *Chinese Physics* **13**.

He, X., Chen, S. and Doolen, G. (1998). A novel thermal model for the lattice Boltzmann method in incompressible limit, *Journal of Computational Physics* **146**: 282–300.

He, X. and Luo, L.-S. (1997). Lattice Boltzmann model for the incompressible Navier-Stokes equation, *Journal of Statistical Physics* **88**: 927–944.

Jonas, L., Chopard, B., Succi, S. and Toschi, F. (2006). Numerical analysis of the average flow field in a turbulent lattice Boltzmann simulation, *Physica A* **32(1)**: 6–10.

Kuznik, F., Vareilles, J., Rusaouen, G. and Kraiss, G. (2007). A double-population lattice Boltzmann method with non-uniform mesh for the simulation of natural convection in a square cavity, *International Journal of Heat and Fluid Flow* **28**: 862–870.

Lai, H. and Yan, Y. (2001). The effect of choosing dependent variables and cell-face velocities on convergence of the SIMPLE algorithm using non-orthohonal grids, *International Journal of Numerical Methods for Heat & Fluid Flow* **11**: 524–546.

Lee, T. and Lin, C. (2005). A stable discretization of the lattice Boltzmann equation for simulation of incompressible two-phase flows at high density ratio, *Journal of Computational Physics* **206(1)**: 16–47.

Li, L., Mei, R. and Klausner, J. (2013). Boundary conditions for thermal lattice Boltzmann equation method, *Journal of Computational Physics* **237**: 366–395.

McNamara, G. and Alder, B. (1993). Analysis of lattice Boltzmann treatment of hydrodynamics, *Physica A* **194(1)**: 218–228.

Mohamad, A. (2011). *Lattice Boltzmann Method - Fundamentals and Engineering Applications with Computer Codes*, Springer London.

Mohamad, A. and Kuzmin, A. (2010). A critical evaluation of force term in lattice Boltzmann method, natural convection problem, *International Journal of Heat and Mass Transfer* **53**: 990–996.

Peng, Y., Shu, C. and Che, Y. (2003). A 3d incompressible thermal lattice Boltzman model and its application to simulation natural convection in a cubic cavity, *Journal of Computational Physics* **193**: 260–274.

Qian, Y. (1993). Simulating thermohydrodynamics with lattice BGK models, *Journal of Scientific Computing* **8(3)**: 231–241.

Qian, Y., D'Humires, D. and Lallemand, P. (1992). Lattice BGK models for Navier-Stokes equation, *Europhysics Letters* **17**: 479.

Succi, S. (2001). *The Lattice Boltzmann Equation: For Fluid Dynamics and Beyond*, Numerical Mathematics and Scientific Computation, Clarendon Press.

Yan, Y. and Zu, Y. (2008). Numerical simulation of heat transfer and fluid flow past a rotating isothermal cylinder - A LBM approach, *International Journal of Heat and Mass Transfer* **51**: 2519–2536.

Yu, Z. and Fan, L.-S. (2009). An interaction potential based lattice Boltzmann method with adaptive mesh refinement (AMR) for two-phase flow simulation, *Journal of Computational Physics* **17**: 6456–6478.

Received: